One-dimensional transient thermal model for predicting module temperatures in ground-mounted fixed-tilt and single-axis tracking PV systems

Brendan Willemse[1a], Johannes Pretorius[1], Michael Owen[1], Arnold Rix[2]

[1]Department of Mechanical and Mechatronic Engineering, [2]Department of Electrical and Electronic Engineering, Stellenbosch University
Private Bag X1, Matieland, 7602, Stellenbosch, South Africa

E-mail: [1a]22635122@sun.ac.za, jpp@sun.ac.za, mikeowen@sun.ac.za, rix@sun.ac.za

Abstract: Accurately estimating the operating temperature of solar photovoltaic modules is crucial for realistic PV system output calculations. This study introduces a computationally efficient one-dimensional transient Finite Difference Method model, developed from first principles, to evaluate the temperature distribution within a PV module throughout the day and predict the operating cell temperature. The model incorporates environmental factors such as plane-of-array irradiance, wind speed, wind direction, ambient air temperature, and the sun's position relative to the PV modules. It is applicable to both ground-mounted fixed-tilt and single-axis tracking configurations, addressing a gap in thermal modelling for tracking PV systems, which are often limited to software packages or neural network models. Model validation against experimental data confirms its accuracy in predicting module temperatures for both configurations.

Keywords PV modelling; Finite Difference Method; ground-mounted; fixed-tilt; single-axis tracking.

1. Introduction

Photovoltaic (PV) systems experience efficiency losses at elevated module operating temperatures, with efficiency decreasing by approximately 0.4% per 1℃ [1]. The diverse range of PV configurations - including open-rack fixed-tilt (FT), open-rack single-axis tracking (SAT), building-attached PV (BAPV), building-integrated PV (BIPV), and floating PV (FPV) - leads to varying module thermal operating conditions, corresponding temperature differences and associated efficiency variations. Accurate estimation of a PV system's operating temperature is critical due to its impact on efficiency and power yield. Consequently, various methods have been developed for precise temperature prediction of PV modules. Empirical correlations for multiple PV configurations have been proposed by studies such as King et al. [2]. Numerical simulations leverage computational power to model complex interactions within PV systems, enabling detailed temperature predictions across diverse scenarios. For example, Hammami et al. [3] developed a one-dimensional (1D) Simulink model to predict cell temperatures for open-rack FT modules. Faiman's empirical model [4] estimates operating module temperatures using configuration-specific heat dissipation factors (HDFs). The King et al. model [2] employs coefficients tailored to different PV types and configurations to predict both module and cell temperatures. A Computational Fluid Dynamics (CFD) model is applied in [5] to simulate module temperature distribution, while an Artificial Neural Network (ANN) approach is used in [6] for temperature prediction in a SAT system, though this method is prone to overfitting and is limited to the specific experimental setup.

This paper presents a computationally efficient 1D transient thermal model capable of predicting module temperatures under varying weather conditions across different PV configurations. The model employs the Finite Difference Method (FDM) applied across the module thickness (front to back surface), with relevant heat transfer mechanisms accounted for via an energy balance at each node. The model incorporates the effects of convection (forced and natural) and radiation heat transfer between the module surfaces and the environment, as well as conduction heat transfer within the module layers. Additionally, it considers the impact of reflected irradiance (albedo) from the ground surface onto the module's back surface and estimates the optical properties of the front glass cover based on the relative sun position. The model is validated against NOCT conditions and measured data from a FT and SAT PV test site.

2. Finite difference model

2.1. Model description

A typical PV module comprises a protective glass layer, two ethyl vinyl acetate (EVA) layers sandwiching a silicon cell, and a tedlar backsheet to safeguard the module's rear surface [3, 7] (Fig. 1). The material properties for each layer, including thickness (t), density (ρ), specific heat (c_p), and thermal conductivity (k), are presented in Table 1. Despite variations in reported material layer properties in literature, these parameters do not significantly vary the total heat capacity of the module [8].

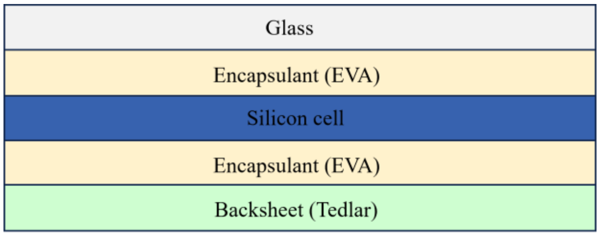

Fig. 1: PV module layer composition

Table 1: PV module layer properties

Material	t [mm]	ρ [kg/m^3]	c_p [J/kgK]	k [W/mK]
Glass	3.2[9]	3000[10,11]	500[10,11]	1.8[10,11]
EVA	0.525[9]	960[10,11]	2090[10,11]	0.35[10,11]
Si Cell	0.18[9]	2330[10,11]	677[10,11]	148[10,11]
Tedlar	0.175[9]	1200[10,11]	1250[10,11]	0.2[10,11]

2.2. Model assumptions

The thermal model is developed based on the following assumptions:

- Thermal properties of module layers are constant.
- The cell and tedlar layers are opaque.
- Optical properties of the layers are considered independent of the radiation wavelength.
- Optical properties of the EVA, tedlar and cell layers are constant.
- Heat transfer across the PV module thickness is one-dimensional.
- Heat conduction from the module to supporting structures is neglected.
- The temperature in each layer is constant over a given time step.
- Initial module temperatures at the first moment of insolation in a day are equal to the ambient temperature.
- Ground surface temperatures are equal to the ambient temperature [7].
- Air is an ideal gas at sea level (atmospheric pressure taken as 101.325 kPa).
- The PV module is approximated as a flat plate for both forced and natural convection.
- Incident solar radiation for a given time step is treated as a uniform heat flux on the front surface of the module.
- The irradiance reaching the cell layer is absorbed, producing electricity and generating heat within the cell layer.
- Absorbed radiation in the glass, EVA and cell layers are uniformly distributed throughout the volume of each layer.
- The albedo factor (θ_{albedo}) is approximated as a constant value of 0.2 [12].
- Albedo from the ground surface is modelled as a fully absorbed heat flux on the bottom surface of the tedlar layer (i.e. $\alpha_{tedlar} = 1$) [3].

2.3. Optical modelling

The optical properties of a solar collector's glass cover significantly affect the collector's performance. The transmissivity (τ), absorptivity (α), and reflectivity (ρ_r) are dependent on the solar beam angle (θ_b) of the incoming radiation [14]. Equation 1 [15] determines the glass transmissivity as a function of the solar beam angle and the refracted angle of irradiance (θ_r), the extinction coefficient (K) taken as $4\,m^{-1}$ [14], and the glass thickness (t).

$$\tau_{glass} = e^{\frac{-Kt}{cos\theta_r}}\left[1 - 0.5\left(\frac{\sin^2(\theta_r - \theta_b)}{\sin^2(\theta_r + \theta_b)} + \frac{\tan^2(\theta_r - \theta_b)}{\tan^2(\theta_r + \theta_b)}\right)\right] \tag{1}$$

The refracted angle (θ_r) of irradiance is determined using Snell's Law, which factors in the index of refraction (n) for air and glass (1 and 1.526 respectively).

$$\theta_r = arcsin\left(\frac{n_{glass}}{n_{air}}\sin(\theta_b)\right) \tag{2}$$

The absorptivity and reflectivity of the glass layer is determined as follows [14]:

$$\alpha_{glass} \approx 1 - e^{\frac{-Kt}{cos\theta_r}}, \tag{3}$$

$$\rho_{r,glass} = 1 - \tau_{glass} - \alpha_{glass.} \tag{4}$$

Table 2 provides the constant optical properties for the remaining PV module layers, including emissivity (ε). The albedo heat flux on the tedlar surface is modelled as fully absorbed.

Table 2: PV module layer optical properties

Material	ρ_r	α	τ	ε
EVA	0.02[10]	0.06	0.92[16]	0.85[10]
Cell	-	0.9[10]	-	-
Tedlar	-	1[3]	-	0.92[10]

2.4. Thermal radiation heat transfer

In the model, it is assumed that losses occur as the light passes through the glass and EVA layers before being fully absorbed by the cell to generate electricity ($\dot{W}_{elec}$) and heat ($\dot{Q}_{gen}$). Radiation exchanges occur between the front (F) and back (B) surfaces of the module with the ground (G) and sky (S) surfaces, which is dependent on the tilt angle (β_{tilt}) of the module. The relative view factors (φ) are calculated from Equations 5 and 6 [17].

$$\varphi_{FS} = \varphi_{BG} = 0.5(1 + cos(\beta_{tilt})) \tag{5}$$

$$\varphi_{FG} = \varphi_{BS} = 0.5(1 - cos(\beta_{tilt})) \tag{6}$$

These view factors are used to determine radiation heat transfer coefficients using Equation 7 between participating surfaces, and corresponding radiation heat transfer rated (Equation 8). Here it is assumed that the sky and ground surfaces, are treated as blackbodies with infinite surface areas. In Equation 8, A refers to the surface area exposed to radiation heat transfer, ε_F is the front surface emissivity and σ is the Stefan-Boltzmann constant. Radiation heat transfer is determined similarly for the other surfaces (FG, BS, BG) as in Equations 7 and 8.

$$h_{rad,FS} = \frac{\sigma(T_F^2 + T_S^2)(T_F + T_S)}{\frac{1-\varepsilon_F}{\varepsilon_F} + \frac{1}{\varphi_{FS}}} \tag{7}$$

$$\dot{Q}_{rad,FS} = h_{rad,FS} A_F (T_F - T_S) \tag{8}$$

The Swinbank correlation [18] is used to determine the effective sky temperature (T_S).

$$T_S = 0.0552 \cdot T_{air}^{1.5} \tag{9}$$

The heat exchange due to the albedo from the ground surface is determined by Equation 10, where H is the plane-of-array (POA) irradiance and A_{PV} is the module surface area:

$$\dot{Q}_G = \theta_{albedo}(H \cdot A_{PV}) \tag{10}$$

The amount of irradiance absorbed by the module's top layers are determined by:

$$\dot{Q}_{abs,glass} = \alpha_{glass}(H \cdot A_{PV}), \tag{11}$$

$$\dot{Q}_{abs,EVA} = \tau_{glass}\alpha_{EVA}(H \cdot A_{PV}), \tag{12}$$

$$\dot{Q}_{abs,cell} = \tau_{glass}\tau_{EVA}\alpha_{cell}(H \cdot A_{PV}). \tag{13}$$

The efficiency of the PV module (η_{PV}) is determined by the Evans expression (Equation 14 [19]), which utilizes the temperature coefficient (β_{ref}), reference efficiency (η_{ref}) and reference temperature (T_{ref}) under Standard Test Conditions (STC) as specified on the manufacturer's datasheet. The power output of the PV module is determined by Equation 15 and the amount of heat generated in the cell layer is determined by Equation 16.

$$\eta_{PV} = \eta_{ref}\left[1 - \beta_{ref}\left(T_{cell} - T_{ref}\right)\right] \tag{14}$$

$$\dot{W}_{elec} = \eta_{PV} H \tag{15}$$

$$\dot{Q}_{gen} = \dot{Q}_{abs,cell} - \dot{W}_{elec} \tag{16}$$

2.5. Convection heat transfer

Equation 17 calculates the convection heat transfer rate from the module surface 'j', where the convection heat transfer coefficient (h_{conv}) is determined from the average Nusselt number ($\overline{Nu}$) and characteristic length (L_c). The air properties of density (ρ), specific heat (c_p), Prandtl number (Pr), and dynamic and kinematic viscosities (μ and ν) are determined at the film temperature (average of surface and ambient temperature). Convection for the back surface is calculated in the same manner. The characteristic length is a function of the module length (L), and width (W) as defined in Equation 18.

$$\dot{Q}_{conv,j} = h_{conv,j} A_j (T_j - T_{air}) \tag{17}$$

$$L_c = \frac{L \cdot W}{2(L + W)} \tag{18}$$

The model accounts for the possibility natural, forced and mixed convection through selection and combination of heat transfer coefficients, as shown in Equation 19 [20].

$$h_{conv} = \begin{cases} \sqrt[3]{h_{conv,forced}^3 + h_{conv,natural}^3}, & if\ 0.1 < \frac{Gr}{Re^2} < 10, \\ h_{conv,forced}, & if\ \frac{Gr}{Re^2} \leq 0.1, \\ h_{conv,natural}, & if\ \frac{Gr}{Re^2} \geq 10. \end{cases} \tag{19}$$

The forced convection heat transfer coefficient is determined using the power law correlation developed in [21] specifically for an inclined flat-plate exposed to winds from various directions. This correlation is also used in [22, 23].

$$h_{conv,forced} = \frac{0.931 c_p \rho}{Pr^{2/3}}\left(\frac{v_{wind} \cdot \nu}{L_c}\right)^{0.5} \tag{20}$$

The natural convection heat transfer coefficient is determined using Nusselt number correlations for an inclined plate derived by Churchill and Chu [24] and Fuji and Imura [25].

$$Ra_{cr} = 10^{8.9 - 0.00178(90° - \beta_{tilt})^{1.82}} \tag{21}$$

If $T_F > T_{air}$ or $T_B < T_{air}$:

$$\overline{Nu} = 0.56(Ra_{cr}\cos(90° - \beta_{tilt}))^{1/4} + 0.13(Ra^{1/3} - Ra_{cr}^{1/3}) \tag{22}$$

If $T_B > T_{air}$ or $T_F < T_{air}$:

$$\overline{Nu} = \left(0.825 + \frac{0.387(Ra \cdot cos\,(90° - \beta_{tilt}))^{1/6}}{(1 + (0.492/Pr)^{9/16})^{8/27}}\right)^2 \tag{23}$$

2.6. Conduction heat transfer

Heat is conducted between the module layers, moving from a region of higher to lower temperature. The rate of conduction heat transfer is dependent on the node temperatures (T_n, T_{n-1} and T_{n+1}), element surface area (A), thermal conductivity and the thickness of the element (L_c) and is determined through application of Fourier's law of conduction as shown in Equation 23.

$$\dot{Q}_{cond,n} = \frac{T_{n-1} - T_n}{\left(\frac{L_c}{A \cdot k}\right)_{n-1} + \left(\frac{L_c}{A \cdot k}\right)_n} + \frac{T_n - T_{n+1}}{\left(\frac{L_c}{A \cdot k}\right)_n + \left(\frac{L_c}{A \cdot k}\right)_{n+1}} \tag{23}$$

2.7. Domain and energy balance discretisation

The model uses an implicit method for calculating nodal temperatures at each time step (Δt), ensuring unconditional stability [20]. In Equations 24-30, 'i' refers to the current time step and Δx represents the element spacing. For nodes in layers where irradiance is absorbed, the contribution of the absorbed irradiance is determined by the volume ratio of the specific node ($\xi_{n,layer}$). The system of linear equations is solved for each node using lower-upper (LU) decomposition in Python, with a temperature convergence error of 1e-3℃.

Front surface energy balance:

$$\left(\dot{Q}_{abs}\xi_F\right)^{i+1}_{\text{glass}} - \dot{Q}^{i+1}_{\text{conv},F} + \dot{Q}^{i+1}_{\text{cond},n+1\to n} - \dot{Q}^{i+1}_{\text{rad},FS} - \dot{Q}^{i+1}_{\text{rad},FG} = \left(\rho \Delta x A c_p\right)_{\text{glass}} \frac{dT}{dt} \tag{24}$$

Interstitial surface nodes with absorption:

$$\dot{Q}^{i+1}_{\text{cond},\, n+1\to n} + \dot{Q}^{i+1}_{\text{cond},\, n-1\to n} + \left(\dot{Q}_{\text{abs}}\,\xi_n\right)^{i+1}_{\text{layer}} = \left(\rho \Delta x A c_p\right)_{\text{layer}} \frac{dT}{dt} \tag{25}$$

Glass-EVA_1 interface surface nodes:

$$\left(\dot{Q}_{abs}\xi_n\right)^{i+1}_{\text{glass}} + \left(\dot{Q}_{abs}\xi_n\right)^{i+1}_{EVA_1} + \dot{Q}^{i+1}_{\text{cond},n+1\to n} + \dot{Q}^{i+1}_{\text{cond},n-1\to n} = \left[\left(\rho \Delta x A c_p\right)_{\text{glass}} + \left(\rho \Delta x A c_p\right)_{EVA_1}\right] \frac{dT}{dt} \tag{26}$$

$EVA_1 -$ Cell interface surface nodes:

$$\left(\dot{Q}_{abs}\xi_n\right)^{i+1}_{EVA_1} + \left(\dot{Q}_{abs}\xi_n\right)^{i+1}_{\text{cell}} - \dot{W}^{i}_{\text{elec}}\,\xi_n + \dot{Q}^{i+1}_{cond,n+1\to n} + \dot{Q}^{i+1}_{\text{cond},n-1\to n} = \left[\left(\rho \Delta x A c_p\right)_{EVA_1} + \left(\rho \Delta x A c_p\right)_{\text{cell}}\right] \frac{dT}{dt} \tag{27}$$

Cell surface energy balance:

$$\left(\dot{Q}_{abs}\xi_n\right)^{i+1}_{\text{cell}} - \dot{W}^{i}_{\text{elec}}\,\xi_n + \dot{Q}^{i+1}_{\text{cond},n+1\to n} + \dot{Q}^{i+1}_{\text{cond},n-1\to n} = \left(\rho \Delta x A c_p\right)_{\text{cell}} \frac{dT}{dt} \tag{28}$$

Cell-EVA interface surface nodes:

$$\left(\dot{Q}_{abs}\xi_n\right)^{i+1}_{\text{cell}} - \dot{W}^{i}_{\text{elec}}\,\xi_n + \dot{Q}^{i+1}_{\text{cond},n+1\to n} + \dot{Q}^{i+1}_{\text{cond},n-1\to n} = \left[\left(\rho \Delta x A c_p\right)_{\text{cell}} + \left(\rho \Delta x A c_p\right)_{EVA_2}\right] \frac{dT}{dt} \tag{29}$$

Interstitial surface nodes without absorption*:*

$$\dot{Q}^{i+1}_{\text{cond},n+1\to n} + \dot{Q}^{i+1}_{\text{cond},n-1\to n} = \left(\rho \Delta x A c_p\right)_n \frac{dT}{dt} \tag{30}$$

EVA_2-Tedlar interface surface nodes:

$$\dot{Q}^{i+1}_{\text{cond},n+1\to n} + \dot{Q}^{i+1}_{\text{cond},n-1\to n} = \left[\left(\rho \Delta x A c_p\right)_{EVA_2} + \left(\rho \Delta x A c_p\right)_{tedlar}\right] \frac{dT}{dt} \tag{31}$$

Back surface energy balance:

$$\dot{Q}^{i+1}_{G} + \dot{Q}^{i+1}_{cond,n-1\to n} - \dot{Q}^{i+1}_{conv,B} - \dot{Q}^{i+1}_{rad,BS} - \dot{Q}^{i+1}_{rad,BG} = \left(\rho \Delta x A c_p\right)_{tedlar} \frac{dT}{dt} \tag{32}$$

2.8. Model verification

This section evaluates the model's independence from spatial and temporal resolution under Nominal Operating Cell Temperature (NOCT) conditions, which is critical for verifying its accuracy. NOCT conditions, as specified in the manufacturer's datasheet [26], are defined as: H = 800 W/m^2, v_{wind} = 1 m/s, $T_{air} = 25$℃, $\beta_{tilt} = 45°$ with air-mass ratio of 1.5 (using $\theta_b = 3.19°$ calculated from the equation in [14]). The model is run with $\Delta t = 60$ s to match the data intervals recorded in the measurement data. Three mesh densities (Coarse, Medium, Fine) with 6, 11, and 21 nodes, respectively, are used to assess the model's sensitivity to mesh resolution in temperature predictions. In contrast, [7] used only 5 nodes, placed at the centre of each layer, in their model.

Table 3: Grid independence study results

Mesh	Element count	T_{cell} [°C]	T_{NOCT} error [°C]	$\dot{E}_{error}$ [W]
Coarse	6	41.11	89.43e-2	14.50e-2
Medium	11	41.11	89.33e-2	7.51e-2
Fine	21	41.11	89.29e-2	4.80e-2

Table 3 compares the predicted PV temperatures (T_{cell}) with the rated module NOCT specification ($T_{NOCT} = 42 \pm 3$℃) and shows the total energy balance error ($\dot{E}_{error}$), which reflects the discrepancy between the energy entering and leaving the PV module. While temperature variations across different mesh resolutions are minimal, finer meshes lead to a lower energy balance error and slightly higher temperatures. This results in the Fine mesh to have the most accurate power output ($\dot{W}_{elec,NOCT}$) prediction of 316.32 W for NOCT conditions (see Table 4). For all meshes, the energy balance error remains below 0.01% of the incoming irradiance. With a 1 s time step, the fine mesh produces a temperature of 41.06°C and an energy balance error of 3.61 W.

This indicates that the 60 s time step is sufficient for accurate temperature predictions. Given its computational efficiency and minimal energy balance error, the fine mesh is selected for the remainder of the modelling process.

3. Data collection and classification

This section describes the test site from which measurement data was collected, for the purpose of validation of model predictions. It is important to clarify that the scope of this study did not include the setup and test work itself (refer to [27] for more details on this). Therefore, only a brief discussion of the measurement equipment at the test site is provided, along with the classification of the measured data based on irradiance quality. POA irradiance (H), wind speed (v_{wind}), wind direction, ambient air temperature and the module back surface temperatures (T_{air} and T_B respectively) were measured on site.

3.1. Mariendahl test site

The ground-based PV configurations from which test data is sourced for this study are located at Mariendahl Farm, outside Stellenbosch, South Africa. Both SAT (modules 1 and 2) and FT configurations (modules 3 and 4) were tested, employing the same PV module type (CS3W-420P) for both setups (see Fig. 2). Table 5 presents the module specifications according to the manufacturer's datasheet [27].

Table 4: CS3W-420P module parameters

	T_{NOCT} [°C]	T_{ref} [°C]	β_{ref} [%/°C]	η_{ref} [%]	$\dot{W}_{elec,NOCT}$ [W]
Data	42 ± 3	25	0.36	19.0	313

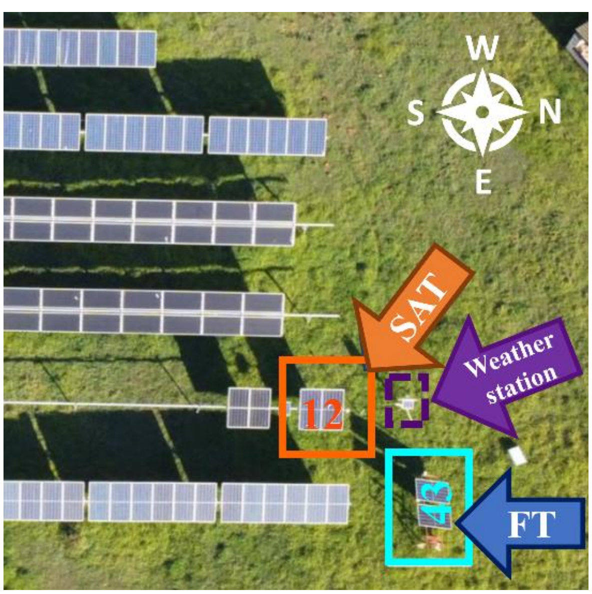

Fig. 2: Mariendahl PV experimental site

The FT configuration features two PV modules positioned at a fixed-tilt angle of 31°, facing North. Similarly, the SAT configuration utilizes two PV modules with tracker running from North-South to track the sun's movement by tilting East-West throughout the day. Both configurations are connected in series to a 136 Ω 4 A resistive load.

Following a setup similar to [5], each module is equipped with two T-type thermocouples affixed to the backside using aluminium tape, positioned centrally and in the corner of the cell. Temperature data for all modules are logged at 1-minute intervals using a Lord TC-Link 200 and recorded via a Lord WSDA Base Station with SensorConnect software. Ambient temperature is measured using a shielded HygroVUE5 digital temperature sensor, while wind speed and direction are captured by a R.M. Young 03002 wind sentry and vane, respectively. POA irradiance is measured using Kipp & Zonen CMP10 pyranometers installed on the structures in-plane with the modules.

3.2. Measured PV data classification

For both PV systems at Mariendahl, measurements were recorded from 2023/04/17 to 2023/08/06, resulting in 72048 and 9758 data points for the FT and SAT configurations, respectively. The SAT configuration experienced issues with accurately tracking the sun on several days, leading to fewer usable data points.

Table 5: Data point count and classifications for the tested PV configurations

PV Config	Complete set	Sunny set	Cloudy set
FT	72048	15413	56635
SAT	9758	7258	2500

The data was categorised into days with steady irradiance readings (Sunny) and days with fluctuating irradiance (Cloudy). This distinction allows for an evaluation of the model's accuracy on clear days and its sensitivity to fluctuations on days with unstable weather (Table 5). This classification is important because it highlights how the model performs under different environmental conditions, which is key to ensuring its reliability. For instance, a model that excels on sunny days but underperforms on cloud-covered days may indicate sensitivity to irradiance fluctuations, guiding areas for further improvement of the model. An example of a Sunny and Cloudy day is shown in Fig. 3.

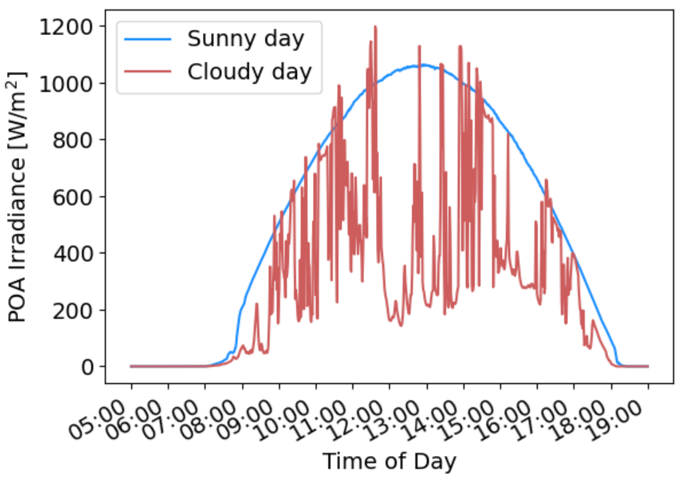

Fig. 3: Sunny and cloudy day comparison for FT configuration

4. Model validation

4.1. *Performance metrics*

To evaluate the model's accuracy and robustness, the root-mean-square error (RMSE), mean absolute error (MAE), mean bias error (MBE), and coefficient of determination (R^2) are employed to compare predicted model temperatures with measured temperatures, as defined in [28]. RMSE and MAE indicate the average magnitude of prediction errors, while MBE reveals any general bias towards over- or under-prediction. (R^2) quantifies the overall correlation between the predicted and measured values.

4.2. *Validation under NOCT boundary conditions*

Initially, the model is validated under NOCT conditions to assess its accuracy against rated module performance under these conditions. Table 6 demonstrates that the thermal model accurately estimates the rated module temperature and associated power output for NOCT conditions (see Table 4).

Table 6: Model predictions for NOCT conditions

	T_{cell} [°C]	$\dot{W}_{elec}$ [W]	T_{NOCT} error [°C]	$\dot{W}_{elec,NOCT}$ error [W]
Model	41.11	316.33	0.89	3.33

4.3. *Fixed-tilt PV validation*

Table 7 presents the performance metrics, demonstrating that the model accurately predicts operating temperatures across a wide range of weather conditions. This is evidenced by the high (R^2) values for the Sunny and Cloudy datasets, with the Sunny dataset showing the highest correlation. The model predicts operating temperatures with an RMSE < 4°C, with the largest MAE and MBE being 2.63°C and -0.98°C, respectively. In comparison, [8] reports MAE and MBE values of 2.61°C and -1.64°C, respectively, for a 5-day period compared to the 111 days utilised in this study. These results indicate that the thermal model reliably predicts operating temperatures for a ground-mounted FT PV configuration under typical transient boundary conditions. The model temperature prediction correlation is shown in Fig. 4.

Table 7: Thermal model accuracy for FT configuration

Dataset	RMSE [°C]	MAE [°C]	MBE [°C]	R^2
Complete	3.95	2.58	-0.77	0.89
Sunny	3.16	2.38	0.03	0.94
Cloudy	4.14	2.63	-0.98	0.85

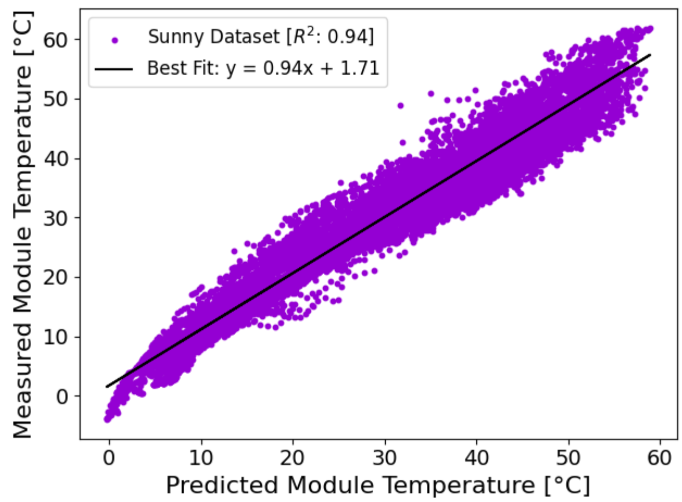

Fig. 4: FT prediction correlation (Sunny dataset)

4.4. *Single-axis tracking PV validation*

The model is now evaluated using measured data for the SAT configuration, with performance metrics detailed in Table 8. The model shows lower RMSE values for both the Sunny and Cloudy datasets compared to the FT configuration, possibly due to having fewer data points. The correlation for these datasets is also sufficiently accurate, with R^2 values of 0.92 and 0.90 for the Sunny and Cloudy datasets, respectively. The MAE and MBE of the model are within an acceptable range. Compared to the RMSE (2.07°C) and MAE (1.45°C) reported for a specialised ANN model [6], the thermal model performs well. The thermal model, therefore, appears capable of estimating operating temperatures for SAT modules with satisfactory accuracy. The model temperature prediction correlation is shown in Fig. 5.

Table 8: Thermal model accuracy for SAT configuration

Dataset	RMSE [°C]	MAE [°C]	MBE [°C]	R^2
Complete	3.08	2.16	1.05	0.91
Sunny	3.02	2.20	0.87	0.92
Cloudy	3.24	2.04	1.58	0.90

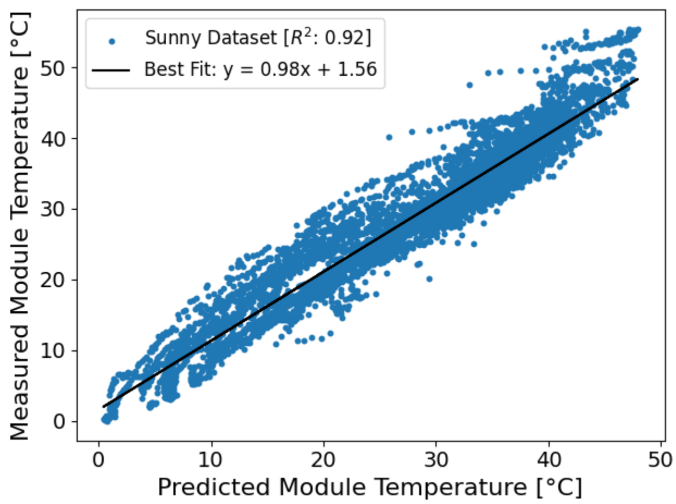

Fig. 5: SAT prediction correlation (Sunny dataset)

5. Conclusion

A one-dimensional transient thermal model for predicting the operating temperatures of ground-mounted FT and SAT PV modules has been developed, verified, and validated against experimental data. The model demonstrates overall error metrics of $R^2 = 0.89$ for FT and $R^2 = 0.91$ for SAT, indicating its capability to predict module temperatures with an RMSE < 4°C across the wide range of operating conditions encountered. While some literature models exhibit similar performance, discrepancies in data quantity used for validation are noted. Future work will focus on expanding the model to FPV applications and for the purpose of comparative studies between different module configurations under identical operating conditions.

Acknowledgements

The authors would like to thank Scatec for providing funding to conduct this research on PV systems at Stellenbosch University.

References:

[1] A. M. K. Abeykoon, G. Aponsu, H. Nadeera, and I. Gunathilaka, "Effect of temperature on the photovoltaic characteristics of polycrystalline silicon solar cells at Hambantota solar power plant," Proceedings of the Solar Asia 2018 Int. Conf. National Institute of Fundamental Studies, Kandy, Sri Lanka, Jan 2018.

[2] D. L. King, W. E. Boyson, and J. A. Kratochvill, "SANDIA Report Photovoltaic Array Performance Model," *Sandia National Laboratories*, Aug 2004. [Online] Available: https://energy.sandia.gov/wp-content/gallery/uploads/043535.pdf

[3] M. Hammami, S. Torretti, F. Grimaccia, and G. Grandi, "Thermal and performance analysis of a photovoltaic module with an integrated energy storage system," *Applied Sciences*, vol. 7, Oct 2017.

[4] D. Faiman, "Assessing the outdoor operating temperature of photovoltaic modules," *Progress in Photovoltaics: Research and Applications*, vol. 16, pp. 307–315, Jun 2008.

[5] M. U. Siddiqui, A. F. M. Arif, L. Kelley, and S. Dubowsky, "Three-dimensional thermal modeling of a photovoltaic module under varying conditions," *Solar Energy*, vol. 86, pp. 2620–2631, Sep 2012.

[6] I. Kayri and H. Aydin, "ANN Based Prediction of Module Temperature in a Single Axis PV System," Proceedings of the 2022 Global Energy Conference (GEC), 2022, pp. 361–367.

[7] F. Nicoletti, M. A. Cucumo, V. Ferraro, D. Kaliakatsos, and A. Gigliotti, "A Thermal Model to Estimate PV Electrical Power and Temperature Profile along Panel Thickness," *Energies*, vol. 15, Oct 2022.

[8] B. Tuncel, T. Ozden, R. S. Balog, and B. G. Akinoglu, "Dynamic thermal modelling of PV performance and effect of heat capacity on the module temperature," *Case Studies in Thermal Engineering*, vol. 22, Dec 2020.

[9] D. Lindholm, J. Selj, T. Kjeldstad, H. Fjær, and V. Nysted, "CFD modelling to derive U-values for floating PV technologies with large water footprint," *Solar Energy*, vol. 238, pp. 238–247, May 2022.

[10] I. Lamaamar, A. Tilioua, and M. A. H. Alaoui, "Thermal performance analysis of a poly c-Si PV module under semi-arid conditions," *Materials Science for Energy Technologies*, vol. 5, pp. 243–251, 2022.

[11] N. Hamrouni, M. Jraidi, and A. Chérif, "Solar radiation and ambient temperature effects on the performances of a PV pumping system," *Revue des Energies Renouvelables*, vol. 11, pp. 95-106, Mar 2008.

[12] Y. Kotak, M. Gul, T. Muneer, and S. Ivanova,"Investigating the Impact of Ground Albedo on the Performance of PV Systems," Proceedings of the CIBSE Technical Symposium, London, UK, Apr 2015.

[13] S. P. Aly, N. Barth, B. W. Figgis, and S. Ahzi, "A fully transient novel thermal model for in-field photovoltaic modules using developed explicit and implicit finite difference schemes," *Journal of Computational Science*, vol. 27, pp. 357–369, Jul 2018.

[14] J. A. Duffie, W. A. Beckman, and N. Blair, *Solar engineering of thermal processes, photovoltaics and wind*, John Wiley & Sons, Inc, 2020. ISBN 9781119540281.

[15] W. De Soto, S. A. Klein, and W. A. Beckman, "Improvement and validation of a model for photovoltaic array performance," *Solar Energy*, vol. 80, no. 1, pp. 78–88, 2006.

[16] A. Reinders, P. Verlinden, W. van Sark, and A. Freundlich, *Photovoltaic solar energy: from fundamentals to applications*, John Wiley & Sons Ltd, 2017, ISBN 9781118927465.

[17] S. Krauter, *Solar Electric Power Generation*, Springer, 2006. ISBN 978-3-540-31345-8.

[18] W. C. Swinbank, "Long-wave radiation from clear skies," *Quarterly Journal of the Royal Meteorological Society*, vol. 89, no. 381, pp. 339–348, 1963.

[19] D. L. Evans, "Simplified method for predicting photovoltaic array output," *Solar Energy*, vol. 27, no. 6, pp. 555–560, 1981.

[20] Y. A. Çengel and A. J. Ghajar, *Heat and Mass Transfer: Fundamentals and Applications*, 6th ed., McGraw-Hill Education, 2020, p. 931. ISBN 9780073398198.

[21] E. M. Sparrow and K. K. Tien, "Forced Convection Heat Transfer at an Inclined and Yawed Square Plate—Application to Solar Collectors," *Journal of Heat Transfer*, vol. 99, no. 4, pp. 507–512, Nov 1977.

[22] S. Kumar and P. M. V. Subbarao, "An improved numerical model to predict the operating temperature and efficiency of solar photovoltaic systems," *Environmental Science and Pollution Research*, 2023. [Online] Available: https://doi.org/10.1007/s11356-023-27650-6.

[23] B. Perovic, D. Klimenta, M. Jevtic, and M. Milovanovic, "A transient thermal model for flat-plate photovoltaic systems and its experimental validation," *Elektronika ir Elektrotechnika*, vol. 25, pp. 40–46, 2019.

[24] S. W. Churchill and H. H. S. Chu, "Correlating Equations for Laminar and Turbulent Free Convection from A Vertical Plate," *International Journal of Heat and Mass Transfer*, vol. 18, pp. 1323–1329, 1975.

[25] T. Fuji and H. Imura, "Natural convection equations," *International Journal of Heat and Mass Transfer*, vol. 15, pp. 755–767, Dec 1972.

[26] Canadian Solar, "Datasheet HiKu CS3W module," 2020. Available:https://www.canadiansolar.com/wp-content/uploads/2019/12/Canadian_Solar-Datasheet-HiKu_CS3W-P_EN.pdf. Accessed: Aug 20, 2023.

[27] J. P. Pretorius and S. Nielsen, "Understanding heat dissipation factors for fixed-tilt and single-axis tracked open-rack photovoltaic modules: experimental insights," *arXiv preprint*, 2023, DOI: 10.48550/arXiv.2312.02373.

[28] S. Zhan and A. Chong, "Data requirements and performance evaluation of model predictive control in buildings: A modelling perspective," *Renewable and Sustainable Energy Reviews*, vol. 142, 2021. [Online] Available: https://doi.org/10.1016/j.rser.2021.110835.